Carbon 228 (2024) 119398

Contents lists available at ScienceDirect

Carbon

journal homepage: www.elsevier.com/locate/carbon

Research paper

Structural and chemical analysis of hard carbon negative electrode for Na-ion battery with X-ray Raman scattering and solid-state NMR spectroscopy

Ava Rajh [a,b,*,1], Matej Gabrijelčič [a,c,1], Blaž Tratnik [c], Klemen Bučar [a,b], Iztok Arčon [b,d], Marko Petric [e,b], Robert Dominko [c], Alen Vizintin [c,**], Matjaž Kavčič [a,b,**]

[a] University of Ljubljana, Faculty of Mathematics and Physics, Jadranska ulica 19, Ljubljana, 1000, Slovenia
[b] Jožef Stefan Institute, Jamova 39, Ljubljana, 1000, Slovenia
[c] National Institute of Chemistry, Hajdrihova 19, Ljubljana, 1000, Slovenia
[d] University of Nova Gorica, Vipavska 13, Nova Gorica, 5000, Slovenia
[e] University of Zagreb, Faculty of Geotechnical Engineering, Hallerova aleja 7, Varaždin, 42000, Croatia

ARTICLE INFO

Keywords:
X-ray Raman scattering
ssNMR
Na-ion batteries
Hard carbons

ABSTRACT

This study explores the structural changes of hard carbon (HC) negative electrodes in sodium-ion batteries induced by insertion of Na ions during sodiation. X-ray Raman spectroscopy (XRS) was used to record both C and Na K-edge absorption spectra from bulk HC anodes carbonized at different temperatures and at several points during sodiation and desodiation. Comparing the π^*/σ^* regions in the C K-edge spectra sp^2/sp^3 hybridization ratio of material was determined. Higher carbonization temperatures led to increased order in graphitic structure and shorter C–C bond lengths. Sodiation caused a decrease in graphitic layer order due to inserted Na ions. Complementary *operando* solid state ^{23}Na nuclear magnetic resonance (ssNMR) studies confirmed the structural changes, while showing pore filling mechanism, which is not observed in *ex situ* measurements, primarily at higher carbonization temperatures. XRS analysis of Na K-edge spectra revealed systematic variations in the solid electrolyte interface (SEI) composition during cycling. Changes in XRS spectra were attributed to both SEI composition alterations, accompanied by the insertion/adsorption of Na ions at defect sites within the carbon structure.

1. Introduction

Sodium-ion batteries (SIBs) represent a promising alternative to widely used Lithium ion batteries. They offer advantages such as high energy density, improved safety and lower environmental impact [1,2]. Na-ion batteries have a similar architecture to Li-ion batteries. During charging and discharging, Na ions shuttle between the cathode and the anode [3,4]. The choice of anode material is critical, as it significantly affects the overall performance of the battery, stability over multiple cycles and the formation of the solid electrolyte interface (SEI) that forms on the anode side during cycling. Unlike Li-ion batteries, where graphite is a common anode material, it is unsuitable for Na-ion batteries since it does not form binary compounds with Na [1,5]. Among the various alternatives, non-graphitizable carbons, also known as hard carbons (HC), are considered leading candidates. Their appeal lies in their low cost, high storage capacity and sustainability. Hard carbons are disordered structures comprising of randomly oriented and curved graphitic domains, defects in the C structure, and nanopores. Even when the raw organic material is heated to high temperatures in a carbonization process, the layers remain disordered and contain some defects that facilitate the insertion of Na^+ ions. The Na capacity generally decreases in HC prepared at temperatures above 1700 °C [6]. With increased temperature of carbonization the C–C bond distances shorten and the amount of defects decreases [7]. The disordered structure gradually transforms into structure more similar to graphite, which is less permeable to the insertion of Na ions.

Hard carbons are characterized by their sp^2/sp^3 hybridization ratio. Mixed hybridization states lead to structural changes such as the bending of graphitic layers and the formation of closed shells and pockets [8,9]. This ratio and consequently the structure of the material are influenced by factors such as pressure and temperature during HC production. Determining the ratio of hybrid orbitals in a material can help in predicting the structural properties, bond types, lengths and strengths as well as the reactivity and conductivity of the material. When the majority of bonds are sp^2 hybridized, structure of hard

* Corresponding author at: Jožef Stefan Institute, Jamova 39, Ljubljana, 1000, Slovenia.
** Corresponding authors.
E-mail addresses: ava.rajh@ijs.si (A. Rajh), alen.vizintin@ki.si (A. Vizintin), matjaz.kavcic@ijs.si (M. Kavčič).
[1] These two authors contributed equally to this work.

https://doi.org/10.1016/j.carbon.2024.119398
Received 17 April 2024; Received in revised form 10 June 2024; Accepted 25 June 2024
Available online 29 June 2024

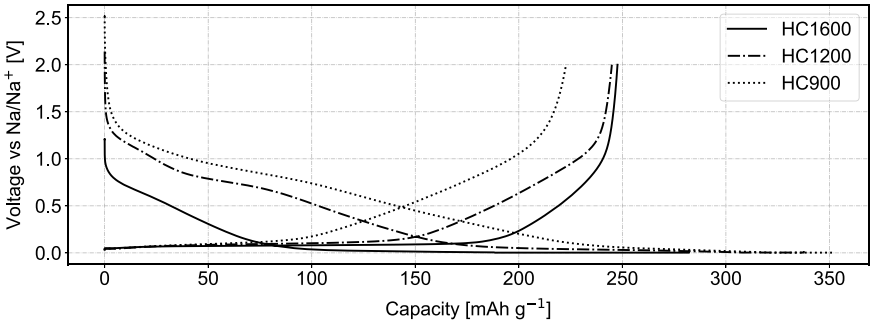

Fig. 1. The sodiation and desodiation profile of Na-ion battery with hard carbon negative electrode carbonized at 900, 1200 and 1600 °C respectively.

carbons closely resembles that of a pure graphite with 6-membered hexagonal rings arranged in large, stacked sheets. As the proportion of sp^3 hybridization increases, the layers become more curved and disordered, leading to an increase in defects and pores between the graphitic layers.

The temperature at which raw organic precursors are carbonized has a significant effect on the sp^2/sp^3 ratio of hard carbons, which in turn affects the mechanism and reversibility of Na insertion and adsorption [10]. This is also evident in our synthesized hard carbons, where the carbonization temperature affects the electrochemical performance (Fig. 1). In general, three distinct regions can be observed on all galvanostatic curves: a sloping region above 0.1 V where the potential changes rapidly, the plateau region between 0.1 V and 0.03 V, characterized by a gradual potential change and a final plateau below 0.03 V where the potential change is slow. In the first sloping region, the capacity is mainly associated with the adsorption of Na ions on the defect sites [1]. The defect sites are typically irregularities in the hexagonal graphitic layer and include vacancies or other elements (such as oxygen and nitrogen) that take the place of individual C atoms [10–12]. They provide space for Na ions to adhere to. The concentration of defects and consequently the prevalence of adsorption increases as the carbonization temperature of the negative electrode material decreases. The capacity in the second and third regions is mostly related to the simultaneous insertion of Na ions between the graphitic layers and the filling of nanopores within the C structure. Depending on the size of the available pores, individual Na ions are stored in smaller pores and larger Na_3 triangle clusters can be found in larger pores [13,14]. In the presence of defects, the growth of large clusters in the pores is limited, as adsorption on defects on the pore walls is more favourable. Different types of storage models exist that explain the process of Na adsorption and insertion into the HC, but further insight is needed to correlate the specific mechanism with a region on the electrochemical discharge curve.

In addition to the Na storage mechanism, the electrochemical performance of hard carbons is influenced by the decomposition of the electrolyte at the C surface, which leads to the formation of the Solid Electrolyte Interface (SEI). SEI acts like an insulating layer that prevents a direct contact of electrolyte with active material, while enabling transport of Na ions to the surface of active material [15]. SEI formation can be divided into three parts. First, Na ions in an electrolyte are transported from the bulk to the outer surface of the electrode, where they lose their solvation shell and migrate to the electrode surface. In the following step, some of the Na ions, impurities and solvent by-products irreversibly react with the electrode material and form the SEI layer. Finally, the remaining ions can pass through the formed layer and insert into the host electrode. The Na insertion and adsorption are reversible as the SEI layer acts as an ion conductor [16]. The SEI is mainly composed of inorganic compounds such as NaF, Na_2CO_3, and Na_2O, as well as alkali and alkyl carbonates, semicarbonates and polymers [17–19]. The SEI layer composition depends on the electrolyte composition and on the state of sodiation due to varying redox potentials of solvents [19–21]. Solubility of the SEI also affects electrochemical performance and can cause cell self-discharge. It has been shown, that the addition of fluoroethylene carbonate (FEC) reduces the solubility of SEI and increases the electrochemical performance and reversibility [22].

The focus of Na-ion battery research is generally on the characterization of Na, due to its central role in the electrochemical reaction [23]. Solid-state nuclear magnetic resonance (ssNMR) [6,14,24,25], X-ray photoelectron spectroscopy (XPS) [16,26], and X-ray diffraction (XRD) [24,27] are commonly employed. A challenge in analysing Na, or Na containing electrodes, is its high reactivity in the atmosphere and its metastable, intermediate, and/or short-lived phases that occur during the electrochemical reactions. ssNMR is particularly valuable for real-time, *in situ/operando* detection in batteries, where the chemical shift and peak structure in NMR spectra provide insights into ionic dynamics, electronic structure, and the local environment of the probed atoms. XPS offers information about the chemical state of elements at the electrode surface and is primarily used to obtain information about the SEI. Besides Na characterization, it is equally important to study the structural properties of HC negative electrode, since it has an influence on the Na insertion processes which in turn affect the electrochemistry of the cell. For this purpose, soft X-ray absorption spectroscopy (XAS) [28] and electron energy loss spectroscopy (EELS) [29] are used. Both provide structural and chemical information about the C atoms in the sample. C K-edge spectra contain information about the C–C distances, layers distances, the hybridization ratios and the chemical environment around the probed atoms, all of which are key in determining the performance and efficiency of battery electrodes. However, the major limitation is the small probing depth, restricting the use of XAS and EELS for surface studies and thin samples.

This is circumvented by non-resonant inelastic X-ray scattering also known as X-ray Raman scattering (XRS). XRS is a well established spectroscopic technique for studying the K absorption edges of light elements in the soft X-ray range where greater penetration depth and bulk sensitivity are required [30–35]. Incident photons in the hard X-ray range (about 10 keV) are inelastically scattered by the target, resulting in a change in the photon's energy and momentum (**q**). The energy transfer can be tuned across the chosen soft X-ray absorption edge and the momentum transfer depends on the scattering angle and the energy of the incoming photons. In a small momentum transfer, the dipole process prevails and the measured XRS spectrum is directly proportional to the soft XAS spectrum. Analogous to XAS, XRS is sensitive to the local chemical environment around the absorbing atom and provides information about its bonding and oxidation states [36–38]. The key advantage of XRS over the conventional XAS in Na-ion battery research is the large penetration depth of hard X-rays. It enables the study of both C and Na K absorption edges in bulk material, without the need for special sample preparation or vacuum conditions. The main limitation of XRS is its relatively small interaction cross-section. The XRS experiment requires a brilliant photon source with a high flux monochromatic beam coupled with a large solid-detection

angle and high spectral resolution limiting the method to undulator beamlines at advanced synchrotron facilities equipped with dedicated XRS spectrometers.

In this work, we have used XRS for the chemical and structural analysis of C and Na in the bulk negative electrode material of the Na-ion battery. The ability to simultaneously monitor chemical structure of Na and the lattice structure of C during sodiation and desodiation cycle of the battery, provides insight into the type of Na insertion mechanism and the influence of the anode structure on the sodiation process. The XRS measurements were complemented by *ex situ* and *operando* NMR, which were used to identify the Na species in the hard carbon electrode and to track the Na insertion mechanism during the sodiation and desodiation.

2. Methods

2.1. Sample preparation

We synthesized hard carbon in a two-step pyrolysis of corncob, as reported in our previous work [7]. The final pyrolysis temperatures were 900 °C, 1200 °C and 1600 °C. After the pyrolysis we ground the obtained hard carbons in a mixer mill (SPEX SamplePrep, Retsch) for 30 min. Prepared materials were denoted as HC900, HC1200 and HC1600.

For the *ex situ* XRS measurements, we prepared hard carbon electrodes with a composition of 95 wt % hard carbon material and 5 wt % polyvinylidene fluoride (PVdF, Aldrich). We dissolved the mixture in N-methyl pyrrolidone (NMP, Aldrich) and ball milled it for 30 min at 300 rpm to obtain a homogeneous slurry. We cast the slurry on a carbon-coated Al foil (Armor, France) using a doctor blade applicator, resulting in a thickness of 150 μm. After drying the coated slurry overnight at 80 °C, we punched out electrodes with a diameter of 15 mm and transferred them to an argon-filled glovebox. We maintained the loadings between 1.5 and 2 mg cm^{-2}.

For electrochemical measurements, we used two-electrode coin-type cells assembled in an argon-filled glovebox with water and oxygen contents below 0.5 ppm. The working electrodes, made of hard carbon, were paired with counter electrodes made of sodium metal (Aldrich, approximately 500 μm thick). The two electrodes were separated by a glass fiber separator (Whatman, GF-A). We employed a 1M $NaPF_6$ electrolyte in EC:DMC (1:1 vol.%) + 2wt% FEC (NP30+FEC). Each cell was filled with 100 μl of electrolyte. We conducted electrochemical measurements using a current of 15 mA g^{-1} within a potential range of 2 V to 0.005 V vs Na/Na^+ (theoretical capacity was calculated based on the model proposed by Bommier [39], which is 301.6 mA h g^{-1}). This corresponded to a rate of C/20. At the end of the sodiation, we applied a constant voltage step at the lower cut-off. This was limited to 15 h or until the current rate dropped below C/100. After disassembling the cells in a glovebox, we washed the cycled electrodes twice in 2 mL of dimethyl carbonate (DMC) solvent to remove excess electrolyte. Finally, we vacuum-sealed all samples in pouch bags with a flat 3.6 μm Mylar window within the Ar glovebox to prevent air exposure.

For *ex situ* NMR measurements, we assembled hard carbon powder materials in a Swagelok-type cell. We assembled the cells in an argon-filled glovebox with water and oxygen contents below 0.5 ppm. We used approximately 20 mg of hard carbon powder as the working electrode and Na metal (Aldrich) as the counter electrode, separated by two GF-A separators wetted by 150 μl of NP30+FEC electrolyte. The cells were sodiated in a voltage range between 2 V and 0.005 V vs Na/Na^+ with a current of 6 mA g^{-1} (C/50). At the end of sodiation, we applied a constant voltage step at the lower cut-off, limited to 15 h or until the current rate was lower than C/100. After disassembling the cells in the glovebox, we recovered the HC powder and placed it into NMR 1.6 mm rotors.

For *operando* NMR measurements, we assembled a battery in the form of an *in-situ* cell following the method described by Pecher et al. [40]. The HC electrode and Na metal were separated by a GF-A separator soaked with approximately 100 μl of NP30+FEC electrolyte. We cycled the in-situ cell in a voltage range between 2 V and 0.005 V vs Na/Na^+ with a current of 15 mA g^{-1} (C/20). At the end of sodiation, we applied a constant voltage step at the lower cut-off, limited to 10 h or until the current rate was lower than C/100.

2.2. XRS

XRS measurements took place at the P01 beamline of the PETRA III synchrotron facility at DESY in Hamburg [41]. The experiments consisted of three main types of measurements: C K-edge XRS, Na K-edge XRS, and an extended C K-edge scan. We used a Si(311) monochromator to tune the incident photon energy and focused the beam on a $200 \times 60\ \mu m^2$ spot on the sample surface. Inelastically scattered photons were analysed by a Johan-type spectrometer consisting of 12 Si(220) spherically bent analysers with a 10 cm diameter in a vacuum sealed movable module intersecting the Rowland circle. Scattered photons were focused on a Medipix3 2D detector (256 × 256 pixels, $55 \times 55\ \mu m^2$). Si(660) diffraction was used, and the analysed emission energy was fixed at 9.7 keV. We fixed the collection angle at a relatively low momentum transfer ($2\theta = 50°$). We positioned the samples on a movable platform allowing movement in x, y, and z directions. The sample surface was inclined 10° relative to horizontal plane to lengthen the path of the beam through the sample.

Before recording each spectrum, we performed a 20 s elastic scan over the 9.684–9.694 keV range, in order to determine the energy resolution, calibrate the energy axis, and isolate regions of interest (ROIs) on the detector. The overall energy resolution obtained was 0.82 eV. For the C K-edge, we scanned the monochromator over the 9.94–10.04 keV range in 0.1 eV steps. We performed three consecutive 50 s scans (0.05 s/step) at the same point on the sample surface to monitor possible changes induced by irradiation. We then moved the beam to a fresh point to avoid radiation damage with prolonged exposure. We summed the spectra from 14 such points to obtain the final C K-edge spectrum. The overall acquisition time per sample was around 30 min. For Na K-edge, we scanned the monochromator over the 10.743–10.813 keV range in 0.2 eV steps. We performed one 1750s scan (5 s/step), then we moved the beam to a fresh spot. We summed three such points for the final Na K-edge spectrum with the overall acquisition time per sample being approximately 1.5 h. Following the C and Na K-edge measurements, we performed an extended energy range scan in order to capture the C EXAFS spectrum. We scanned the incident energy over 9.84–10.44 keV range in 1 eV steps. As before, we performed three consecutive scans (1s/step) at each point on the sample surface before moving to a fresh point. The final spectrum was an average of 3 to 5 points, accumulating an acquisition time of 1.5 to 2.5 h.

Due to the point-to-point focusing of spherical analysers, photons scattered from different depths of the sample were focused on different positions on the 2D detector. This property allowed us to isolate the signal from the sample environment and other unwanted contributions and provided depth sensitive information about our samples. To further optimize signal to noise ratio, we identified new ROIs on the detector with the help of an elastic scan each time the beam was moved to a new spot on the sample surface. Additionally, we recorded the metallic Na K-edge spectrum separately at the ID20 beamline of ESRF synchrotron. We kept the sample in a pouch bag sealed within an Ar glovebox for the duration of the measurement. We performed the measurement at two different momentum transfers and summed over both after background subtraction.

To extract the corresponding soft XAS spectrum, we subtracted the valence Compton contribution from the total measured XRS spectrum. By selecting a low momentum transfer regime, the Compton peak maximum was positioned around 100 eV. This was far away from the energy range of our measurement and we could simplify the background as a linear function obtained from the pre-edge region. After linear background subtraction, we normalized the data at 60 eV above the edge using the Larch software package [42].

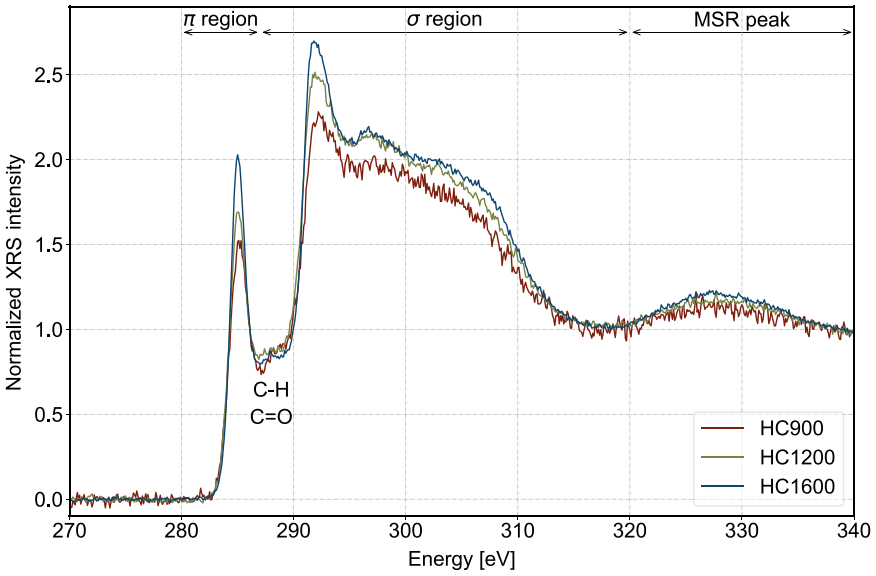

Fig. 2. Variation in C K-edge XRS spectra of hard carbons carbonized at three different temperatures. The labels above the spectra describe the three distinct regions of the C K-edge. (For interpretation of the references to colour in this figure legend, the reader is referred to the web version of this article.)

2.3. NMR

For solid-state magic angle spinning (MAS) *ex situ* NMR spectra, we recorded fully sodiated and desodiated hard carbon electrodes on a 600 MHz VNMRS spectrometer (Agilent Technologies) using a 1.6 mm Triple Resonance HXY FastMAS Varian Probe. The shift axis in all spectra was referenced using adamantane as an external secondary reference, with the ^{1}H signal set to 1.85 ppm. We can consider the reported shifts to be accurate to within ±0.5 ppm. Larmor frequencies of ^{23}Na and ^{19}F nuclei were 158.538 MHz and 564.298 MHz respectively. We set the sample MAS frequency to 20 kHz and recorded ^{23}Na spectra with an excitation pulse duration of 0.5 μs, accumulating 20 000 scans with a 0.1 s delay between scans.

We recorded ^{19}F spectra using a Hahn echo pulse sequence with $\pi/2$ and π pulses with durations of 2.8 μs and 5.6 μs, respectively, accumulating 200 scans with a 10 s delay between scans. By rotating the sample at a magic angle (MAS) to the direction of the magnetic field, we achieved higher resolution in the diamagnetic part of the spectrum around 0 ppm. This allowed resolution of the individual contributions through deconvolution using ssNake software [43].

For solid-state *operando* NMR spectra, we recorded spectra on a Bruker AVANCE NEO 400 MHz NMR spectrometer using an ATMC IN SITU NMR 400 SB Probe. The shift axis in all spectra was referenced using NaCl as an external secondary reference, with the ^{23}Na signal set to 7.2 ppm. The Larmor frequency of ^{23}Na nuclei was 105.845 MHz, and we did not rotate the samples during measurement. We recorded ^{23}Na spectra using an excitation pulse with a duration of 4.75 μs, accumulating 16 384 scans with a 0.05 s delay between scans.

3. Results and discussion

3.1. C K-edge

Initially, C K-edge spectra of pristine anode materials were recorded. A comparison of the C K-edge spectra of the pristine materials in Fig. 2 reveals that both the π^* resonance and the features of the σ^* band become more pronounced with an increased temperature of carbonization. The change is attributed to the structural changes in the material, as its crystallinity and periodicity increase and the amount of sp^3 hybridization decreases.

In sp^2 hybridized C, the overlap of two sp^2 hybridized orbitals from adjacent atoms within the same plane leads to the formation of two molecular orbitals (MO): a bonding σ orbital and an empty σ^* anti bonding orbital. They produce an exceptionally rigid and strong 2D structure of hexagonal rings. An overlap between unhybridized $2p_y$ atomic orbitals of adjacent planes forms a bonding π and an anti bonding π^* orbitals which act as weakly interacting covalent bonding between the layers. In contrast, in a purely sp^3 hybridized crystal structure, each C atoms is bound to four of its neighbours with a σ bond, resulting in an extremely rigid 3D structure. This implies that the absorption cross section from 1s core level to the π^* antibonding state is proportional to the number of sp^2 bonded atoms in a material. In C K-edge spectra, a sharp resonance around 285 eV is a result of 1s to π^* transition and a broad band above 290 eV is mostly a result of 1s to σ^* transitions from both sp^2 and sp^3 hybridized C atoms. Part of the intensity between these main features is attributed to the presence of C−C and C=O bonds. These are indicative of defects and oxygen contamination in the pristine material [44–47]. The amounts of sp^2 hybridized C atoms for pristine HC, carbonized at different temperatures, were determined by comparing the ratio of areas under the spectra, centred on π^* and σ^* bands. The window from 283 to 286 eV was assigned to the π^* resonance and the window from 286 to 320 eV contained the broad σ^* band. The ratio of these two components, when normalized to the value where the sample contains only sp^2 type bonded C atoms (like a perfect graphite crystal), describes the percentage of sp^2 bonded atoms in a sample [48,49]. This method, while known to overestimate the amount of sp^3 bonded atoms due to overlap of π^* and σ^* features [28,49], still allows for observing general trends. Comparing the π^*/σ^* ratios for each of the investigated pristine hard carbon materials in Fig. 3 revealed a slight shift towards higher values, indicating an increase in sp^2 bonded atoms with higher carbonization temperatures. Assigning 100% to the hard carbon carbonized at 1600 °C, the relative sp^2 amounts in HC900 and HC1200 samples were found to be 94.9% ± 1.5% and 93.2% ± 1.3% respectively, and within experimental margins of each other. The general increase in the concentration of sp^2 hybridized C atoms with higher carbonization temperature is consistent with the trend previously observed using EELS spectroscopy [7]. In this case, the shift is less pronounced. This might be attributed to the large difference in the probing volume. While some orientation effects might be introduced in the EELS result, all possible orientations of the graphitic planes are averaged in the large volume probed by XRS technique. Additionally, the σ^* region appears suppressed at lower carbonization temperatures, and the two distinct

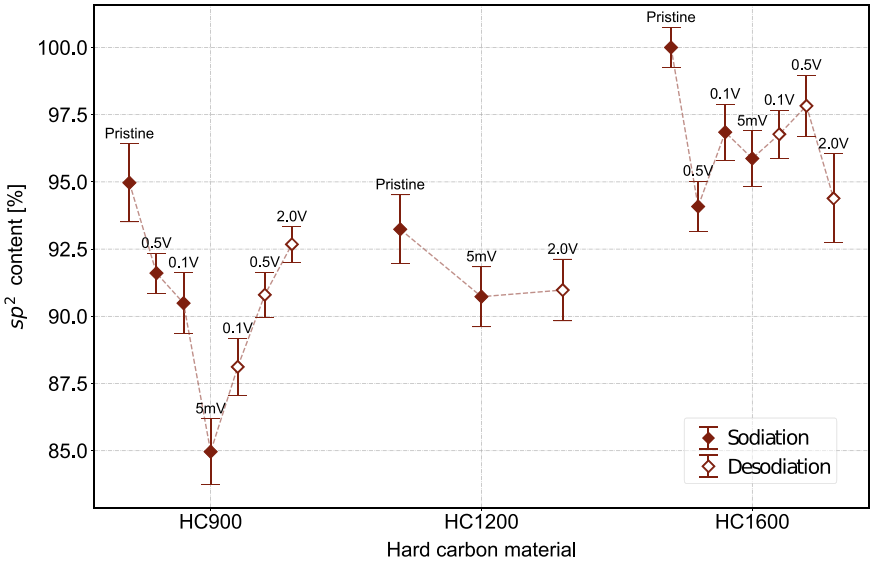

Fig. 3. sp^2 hybridized C content in pristine hard carbons carbonized at three different temperatures and in their respective *ex situ* negative electrodes stopped during the sodiation and desodiation of the battery. The dashed line connecting the points is shown to group the samples with the same HC material, the label denotes the voltage at which the battery was stopped, full markers represent sodiation, empty represent desodiation. The relative intensities were normalized to the intensity of the pristine HC1600 sample with the highest amount of sp^2 hybridized C.

peaks at 292 and 306 eV, resultant from σ^* splitting due to π^* bond conjugation, become less defined.

Next we investigated the structural changes during the battery cycling. For each negative electrode material, a series of static (*ex situ*) measurements were performed on batteries halted at specific points during sodiation and desodiation of the battery. For the HC900 and HC1600 materials, the batteries were stopped at 0.5 V, 0.1 V, 0.005 V during sodiation and at 0.1 V, 0.5 V, and 2 V during desodiation. The HC1200 material was only stopped at the end of sodiation (0.005 V) and the end of desodiation (2 V). This resulted in 7 (or 3 for HC1200) distinct C spectra for each battery. Following the previously described procedure, the amount of sp^2 hybridized C atoms was determined for each point of the battery cycle. A consistent trend can be observed for the HC900 sample on Fig. 3, with the sp^2 decreasing with sodiation and increasing with the following desodiation. The structural changes are caused by the reversible bending of the graphitic layers to accommodate the Na ions that insert between the layers, and a local deformation of the planar C structure where Na ions adhere at the defect sites. A more consistent sp^2 content without any systematic structure changes over the battery cycle is observed for the HC1600 material. In case of higher carbonization temperatures, pore filling prevails over insertion and adsorption. The effect of Na clusters in nanopores on the HC structure cannot be observed in the *ex situ* samples. The metastable Na ions that fill the pores self desodiate over a course of a few hours after the potential is no longer applied to the battery, and the changes to the HC structure are already reversed at the time of the XRS measurement [50]. The small variations in the observed sp^2 contents can also be a result of variation between the individually prepared *ex situ* samples. The HC1200 sample showed the least change in sp^2 content during cycling, but the limited number of data points recorded for this set may obscure any broader trend that can be seen in HC900 and HC1600.

3.1.1. Multiple scattering resonance

The spectral feature around 330 eV is attributed to the multiple scattering resonance (MSR), a phenomenon representing the energy of a standing wave formed when an excited photoelectron is scattered from the second nearest neighbour to the excited atom [48]. According to previous studies, the intensity of the peak is proportional to the degree of order in the C structure [28,51]. A broader bond length distribution and a higher sp^3 concentration typically result in a less intense MSR peak. In addition, the energy of this feature is inversely proportional to the square of the radius of the second coordination shell [52,53].

A Gaussian function was used to model this peak on top of a step background function and extract its energy and intensity and the fit can be seen in Figs. A.16 and A.17. The intensities of the MSR peaks are presented in Fig. 4(a). The observed trend mostly aligns with the results obtained from the π^*/σ^* ratios in Fig. 3. With an increase in carbonization temperature, the intensity of the peak grows indicating a more ordered C structure, an increase in π bond conjugation and an overall higher sp^2 concentration. The changes are also observed during the sodiation/desodiation cycle, where the increased presence of Na ions between the C layers disrupts the formation of π bonds between layers and reduces the amount of sp^2 hybridization.

The energy of MSR peak was used to monitor the changes in the nearest neighbour C–C bond lengths (R_1) in the HC materials. A quantitative analysis was performed using the following relation [48]:

$$R_2 = \sqrt{K/E_{MSR}}, \quad (1)$$

where E_{MSR} is the energy of MSR peak, R_2 is a second coordination shell radius which is proportional to the first coordination shell radius (R_1) by $R_2 = 2R_1\sin 60°$ and K is an empirical constant. K was determined from the experimental E_{MSR} value of the pristine HC1600 sample and assuming the nearest neighbour C–C distance equals that of a perfect graphite (R_1 = 1.4202 Å). The calculated bond lengths are plotted in Fig. 4(b) and show a systematic decrease with an increase in carbonization temperature. This is consistent with previously shown increase in the amount of sp^2 hybridized C atoms, whose nearest neighbour C–C bonds are shorter than the one in sp^3 hybridized C atoms. Within the precision of our measurements, no systematic variation in bond lengths was observed for *ex situ* negative electrodes during battery cycle.

3.2. C EXAFS

We used XRS to record the EXAFS spectra at the C K-edge to measure the distances between neighbouring atoms and the disorder in hard carbon materials. EXAFS spectra were recorded for pristine anode materials carbonized at 900 °C and 1600 °C, as well as for their respective *ex situ* negative electrode after sodiation. All recorded spectra contained a substantial contribution from the oxygen K-edge around 530 eV. The presence of the jump in the middle of C EXAFS oscillations, limited the usable range of the recorded spectra. To

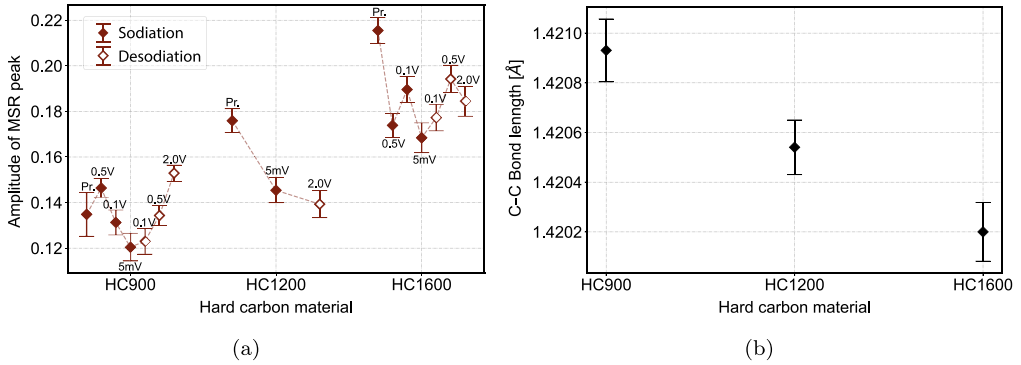

Fig. 4. (a) The MSR peak intensity of *ex situ* negative electrodes stopped during the sodiation/desodiation cycle of the battery. The dashed line connecting the points is shown to group the samples with the same HC material, the label denotes the voltage at which the battery was stopped. Full markers represent sodiation, empty represent desodiation. (b) Average C–C bond length in pristine hard carbons carbonized at three different temperatures The energy of the MSR peak of pristine HC1600 sample was taken as a reference and assigned the nearest neighbour bond length of 1.4202 Å.

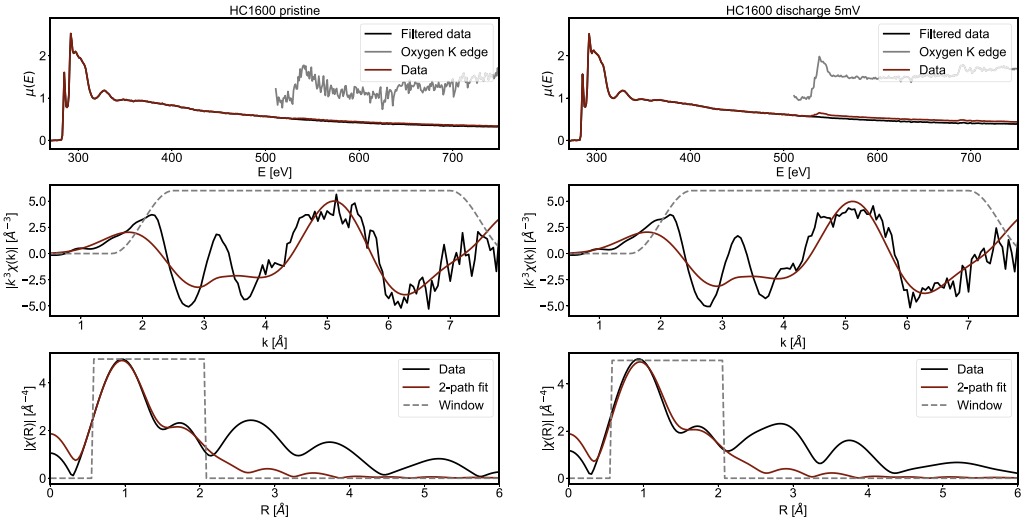

Fig. 5. Top: Normalized C EXAFS spectra of pristine and fully sodiated HC anode carbonized at 1600 °C and the Oxygen K-edge, which was removed from the spectra. Middle: EXAFS spectra in k space along with a fit with two scattering paths. Dotted line represents the window used for the fourier transform. Bottom: EXAFS spectra in R space along with fit with the first two scattering paths. The window represents the region used in a fit.

address this, we decided to remove the contribution from the O K-edge and focus only on the spectrum up to the edge. A normalized oxygen spectrum was subtracted from the entire C EXAFS, providing a smooth background above the 530 eV, which was used to stabilize fit with spline background function, as can be seen in Fig. 5. A smooth spline function ($\mu_0(E)$) was matched to the normalized spectrum using the AUTOBK algorithm in the Larch software package [54] from 50 to 240 eV above the edge. This algorithm is designed to eliminate low frequencies corresponding to distances smaller than the nearest neighbour distance in our system. A cutoff of R = 0.6 Å was used. The energy axis of the EXAFS spectra was converted to electron momentum space, which can be seen in Fig. 5, setting the zero in energy (E_0) for scattered electrons to 289 eV. Contributions to the spectra above k = 7.5 were disregarded due to previously mentioned oxygen edge. A Fourier transform was applied to obtain the $\chi(R)$. Two main peaks were identified in the spectra, which are attributed to the contributions from the first and second coordination shell. The amplitude of $\chi(R)$ is most pronounced at the first neighbour shell around 1.42 Å.

A pure graphite model was utilized to simulate the theoretical multiple scattering paths simulations using FEFF6 [55]. The experimental spectra were fitted based on the EXAFS equation only up to the second coordination shell, specifically between R = 0.6 Å and R = 2.1 Å. The number of atoms in the first and second coordination shells was fixed to the known values of 3 and 6, respectively. The free parameters in the fit included the distance between the absorbing and scattering atoms (R_i) and the width of the Gaussian distribution (or the Debye–Waller factor, σ_i). The constant S_0^2 parameter, which accounts for multielectron excitations was fixed to 0.9. The distance from the absorber to the first and second nearest neighbour in all samples was calculated to be around 1.375 Å and 2.43 Å respectively, slightly shorter than the reported literature values for graphite, which are of 1.42 Å and 2.46 Å respectively [56]. The fit in *k* and R space is shown in Fig. 5. The results of fitting can be found in the Table 1. The tiny changes in the average C–C bond length obtained from the energy of the MSR peak are below the uncertainty of the EXAFS near neighbour distances, showing virtually no change within the first and second coordination shell for HC materials carbonized at different temperatures. The same holds for the results of the pristine and fully sodiated negative electrode where relatively large uncertainties prevent observation of any significant changes induced by the insertion or adsorption of Na ions. However, the Debye–Waller factors, indicative of bond length variation, were observed to be smaller for both anode materials carbonized at 1600 °C implying that with an increase in carbonization temperature, the structure is less disordered. The fact that the out of plane scattering paths are not prominent and we were unable to fit them with a simple graphite model, shows that EXAFS only observes relatively stiff and rigid planar graphitic ring structure. No obvious contributions from the C–Na bonds are observed, as the Debye–Waller factor for them would be too big.

Table 1
The calculated best fit parameters for all recorded samples.

Sample	S_0^2	R_1 [Å]	R_2 [Å]	σ_1^2 [Å^2]	σ_2^2 [Å^2]
HC900 pristine	0.9	1.372(5)	2.43(2)	0.0059(9)	0.014(3)
HC900 sodiated	0.9	1.375(5)	2.43(2)	0.0059(9)	0.014(4)
HC1600 pristine	0.9	1.380(3)	2.43(2)	0.0050(6)	0.010(2)
HC1600 sodiated	0.9	1.376(5)	2.43(1)	0.0052(9)	0.010(2)

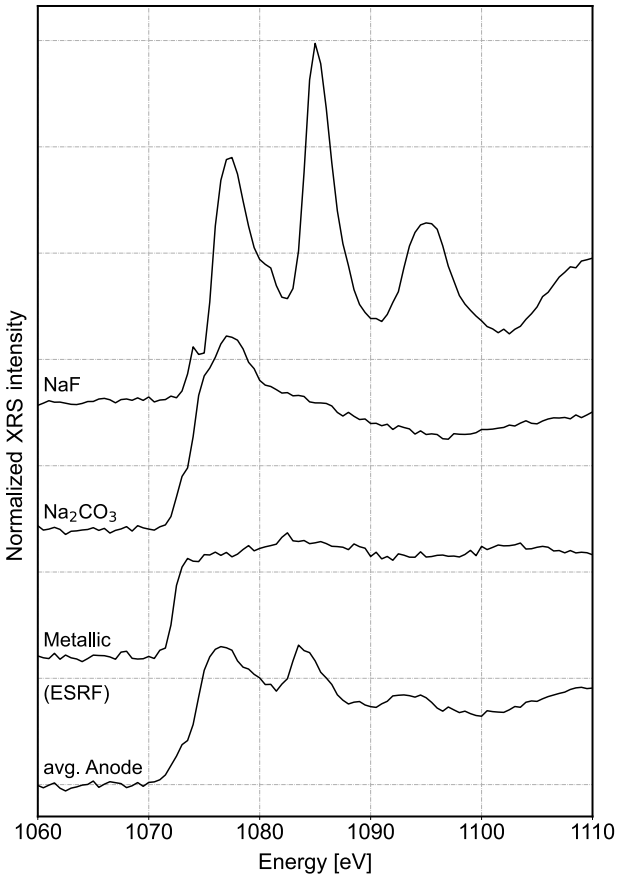

Fig. 6. Na K-edge XRS spectra of reference standards along with an averaged Na spectrum over all recorded samples.

3.3. Na K-edge

Na K-edge spectra were recorded for Na_2CO_3 and NaF reference samples predicted to form a solid electrolyte interface (SEI) and metallic Na, since it has been previously suggested, that Na forms quasi metallic clusters in the nanopores [13]. They are compared to each other in Fig. 6. Next, Na K-edge XRS spectra were recorded *ex situ* on all pre-cycled negative electrodes HC900 and HC1600 in order to monitor the insertion mechanism of Na in-to the hard carbon negative electrode and the formation of the SEI. The two HC carbonization temperatures were selected based on the largest expected difference among the samples. Na K-edge spectra of all samples can be seen in Fig. A.13. A direct comparison of the spectra from metallic Na and other references, along with a linear combination fit (LCF) analysis on the *ex situ* negative electrodes revealed, that most of the Na signal in the anode originates from a combination of NaF and Na_2CO_3. An example of such fit can be seen in Fig. 7(a). These two compounds are the main components of the SEI, which is formed during sodiation, and are present throughout the anode's bulk. The fit with two components in Fig. 7(a) is generally a good one, but shows a discrepancy in the feature between 1080 and 1085 eV. To explain the discrepancy, we performed time dependent density functional theory (TDDFT) calculations of Na in different environments. The calculation details are described in Appendix A.1. They suggest that the XAS spectrum of Na ion inserted between graphitic layers has a similar profile as the measured Na_2CO_3, with a more prominent feature between 1080 and 1085 eV as can be seen in Fig. 7(b). The discrepancy in the two component LCF fit is therefore attributed to the presence of additional Na species corresponding to the inserted Na ions.

The amount of NaF is stabilized by the first measured point [57], which was also confirmed by *ex situ* ^{19}F ssNMR in Fig. A.15. Any variations of the relative intensity of the two components used in the LCF analysis throughout sodiation and desodiation are attributed to a simultaneous formation and subsequent dissolution of Na_2CO_3 in the SEI and Na insertion between graphitic layers. Since the theoretical calculations showed that the spectrum of inserted Na ions resembles the Na_2CO_3 one, the two contributions cannot be resolved and the Na_2CO_3 component in the LCF fit can be considered as a sum of both. The relative intensity of Na_2CO_3 LCF component during sodiation and desodiation is shown in Fig. 8. We observe that the amount of Na_2CO_3 increases during sodiation, reaching the maximum NaF : Na_2CO_3 ratio of about 1 : 10 in the case of HC900, then returns to the starting value during desodiation. A similar trend is also observed for HC1600 material. An XPS study of a SEI layer in *ex situ* negative electrodes with HC900 material (Fig. A.14) revealed a similar trend, where the amount of Na_2CO_3 increased during sodiation and decreased again during desodiation. The main observed difference between HC900 and HC1600 is the relative intensity of Na_2CO_3 component at the beginning and the end of the cycle. Since this component corresponds to the cumulative signal of both, Na_2CO_3 from the SEI and Na–C inserted species, the difference is attributed to the different ratio between these two species, which might depend on the HC carbonization temperature.

3.4. NMR

To confirm and quantify the changes in the composition of the SEI observed in XRS spectra, *ex situ* ^{23}Na NMR was conducted on a fully sodiated and desodiated HC900 and HC1600. Fig. 9 shows the spectra and deconvolution plots for HC900. The blue colour highlights the presence of the electrolyte signal, which was present in the electrode. The contributions of Na_2CO_3 and NaF are visible in the spectrum. The chemical shifts and integrals for all three components are presented in Table 2. The ratio of NaF to Na_2CO_3 contribution in HC900 is 1:48 for a fully sodiated state and 1:25 for a desodiated one. All three contributions present in HC900 are also present in HC1600. The ratios of NaF to Na_2CO_3 contribution are 1:29 and 1:6.5 for a fully sodiated and desodiated states of HC1600 respectively. This indicates an increase in the amount of Na_2CO_3 present in the SEI during sodiation in agreement with the XRS results. An overall change of SEI composition with carbonization temperature is also observed, with HC1600 containing about 2 times lower ratio of NaF to Na_2CO_3 than HC900. The differences in the amounts of the electrolyte signal observed in the NMR spectra may be due to the process of extracting the sample from the cell, which causes the electrolyte to be distributed differently across the electrode in different cells. The absolute values of the NaF to Na_2CO_3 however are much larger than the results from XRS, which is attributed to the preparation methods for the *ex situ* electrodes, which were washed with DMC for the XRS and XPS measurements. Since Na_2CO_3 is partly soluble in the electrolyte, the process of washing the sample could alter the ratios of Na_2CO_3 to NaF.

Finally, *operando* NMR was performed on HC900 and HC1600 negative electrode to correlate the Na insertion with the changes in the graphite lattice observed in XRS data. The resulting spectra are shown on Figs. 10 and 11. In HC900, two signals are detected from the beginning. At 1130 ppm a signal from metallic Na and around 0 ppm a signal from the electrolyte. The electrolyte peak expands during sodiation, because SEI is also formed in this region. During sodiation

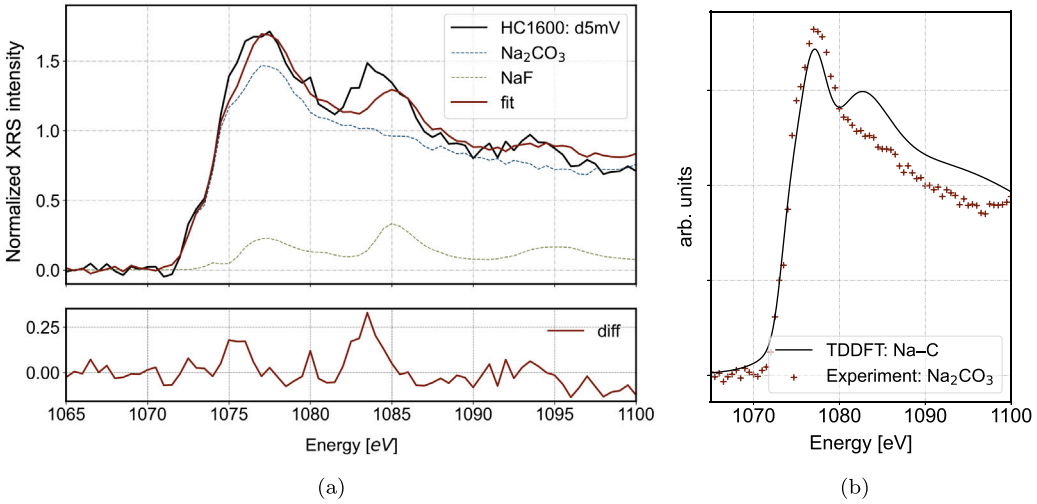

Fig. 7. (a) An example of a LCF fit with two standards, that best describe the measured spectrum from the *ex situ* anode. Hard carbon was carbonized to 1600° and the battery was discharged to 5 mV. (b) TDDFT calculated spectrum of Na inserted between carbon layer compared to the experimental Na_2CO_3 one.

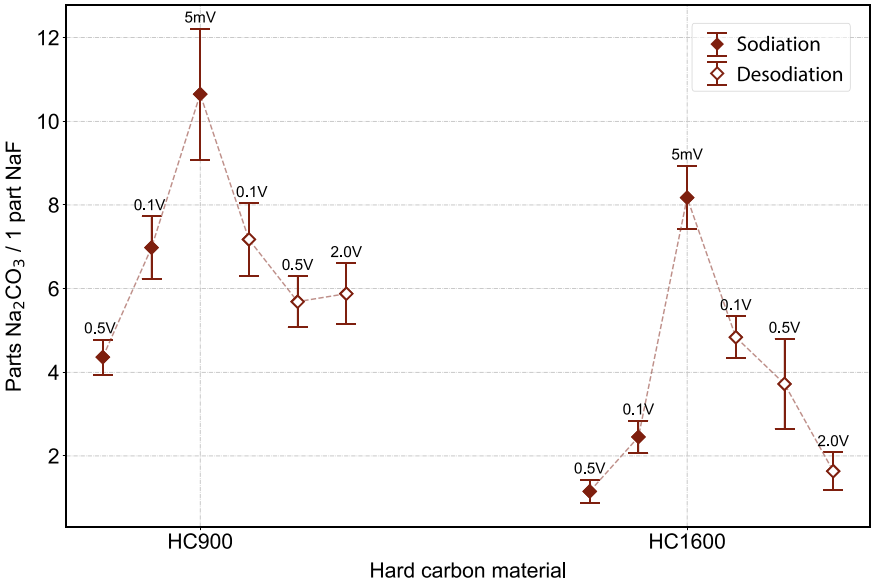

Fig. 8. Relative intensity of the LCF component corresponding to the Na_2CO_3 in *ex situ* negative electrodes in relation to a fixed NaF content. Pristine hard carbons were carbonized at three different temperatures. The dashed line connecting the points is shown to group the samples with the same HC material, the label denotes the voltage at which the battery was stopped. Full markers represent sodiation, empty represent desodiation.

Table 2
The calculated chemical shifts and integral % of individual components, for all recorded *ex situ* samples measured with ^{23}Na NMR.

Sample	NaF		Na_2CO_3		Electrolyte	
	Shift [ppm]	Integral %	Shift [ppm]	Integral %	Shift [ppm]	Integral %
HC900 d5mV	6.50	1.79	−3.75	85.75	−10.51	12.46
HC900 c2V	6.56	2.61	−11.81	65.08	−10.89	32.31
HC1600 d5mV	6.72	3.12	0.09	90.96	−10.75	5.92
HC1600 c2V	6.28	6.41	−7.16	41.44	−10.96	52.15

at a potential of 0.1 V vs Na/Na^+, an additional signal appears at 400 ppm, which then disappears into the noise region at 5 mV vs Na/Na^+. Upon desodiation, this signal reappears, reaches a maximum at 0.1 V vs Na/Na^+ and decays again upon recharging at 2 V vs Na/Na^+. Additionally, a different signal phase at the transition between sodiation and desodiation of the battery is detected around 0 ppm, which may indicate a different conductivity during the sodiation and desodiation process. During the low voltage region of the electrochemistry, the resonance shifts to positive frequencies. This indicates that the local structural and/or electronic environment of the Na ions changes as more Na is incorporated into the structure at lower potentials. Larger shifts indicate an increase in the Na 2s density of states at the Fermi level, implying that the Na species becomes increasingly metallic during this period of electrochemistry. Na ion insertion occurs between disordered graphitic layers with appropriate spacing, followed by further insertion into nearby empty environments near the defects. This insertion results in a more disordered graphite structure. As the C is reduced, the Na^+–C interaction gradually becomes less ionic [50].

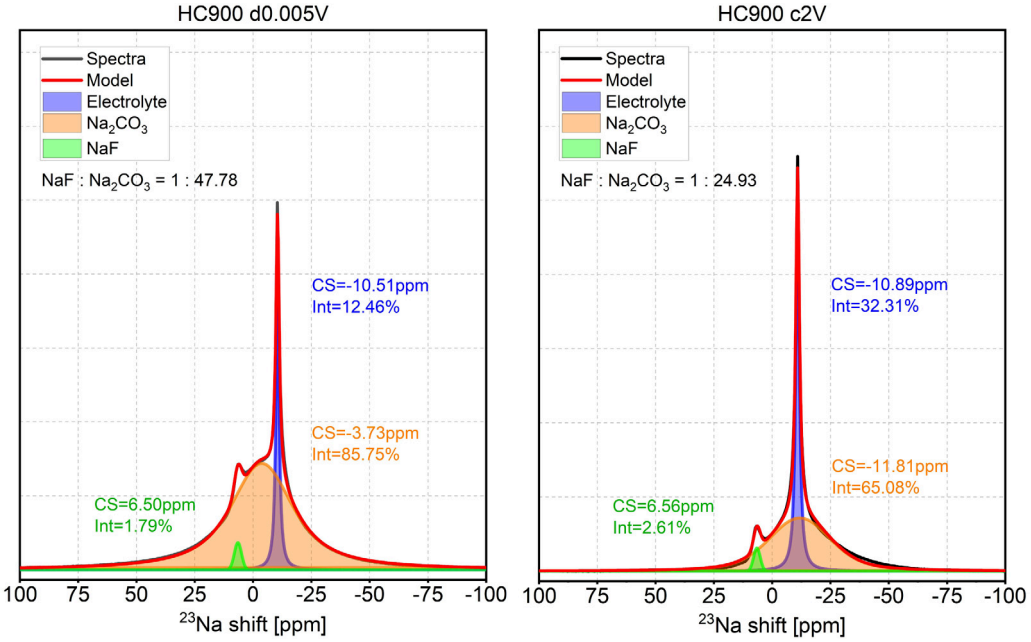

Fig. 9. *Ex situ* solid-state ^{23}Na spectra of fully sodiated (left) and desodiated (right) HC900 powder along with a best 3 component fit. (For interpretation of the references to colour in this figure legend, the reader is referred to the web version of this article.)

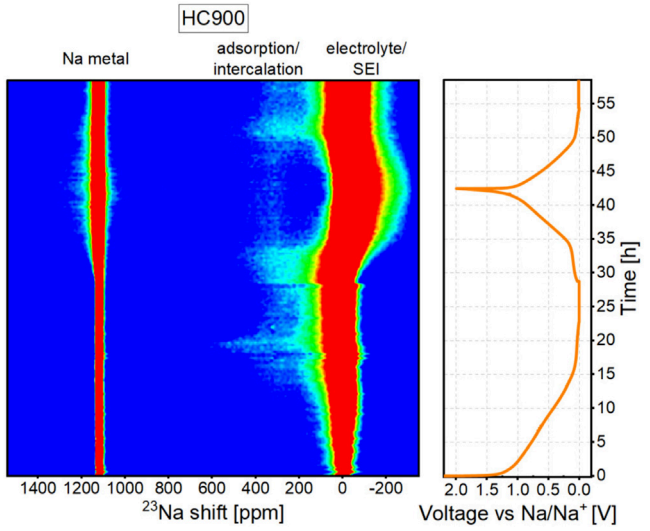

Fig. 10. Spectrum of solid-state ^{23}Na *operando* NMR on a Na-HC900 half-cell at 90° orientation of electrodes with respect to the external magnetic field of the spectrometer. Electrochemistry is added on the right.

In contrast to HC900, a strong signal is detected in HC1600 around 800 ppm during sodiation at 5 mV vs Na/Na$^+$. This signal is attributed to the accumulation of quasi-metallic clusters during the Na ion pore-filling phase [50]. Where pores are large enough, extended Na clusters form, which are more metallic in nature. The shift stabilizes at the point where the majority of Na ions accumulate in pores with a similar chemical environment. This also leads to an increase in NMR signal as more Na ions contribute to the signal. The metastable Na ions that fill the pores in the HC1600 require an electrostatic potential to remain in the pores and the absence of the applied potential causes the Na ions to self desodiate over the course of a few hours. They are no longer present in the *ex situ* NMR samples and the signal at 800 ppm was not detected in a fully sodiated state. Therefore they do not influence the HC structure in agreement with the structural analysis from the C K-edge XRS spectra. During sodiation, the processes occur in a specific sequence (adsorption, insertion, pore filling). In contrast, during desodiation, the processes occur in reverse order (pore filling, insertion, adsorption). Notably, the pore filling signal disappears immediately as the clusters are desodiated first. HC1600 shows a smaller peak broadening around 0 ppm than HC900. This could be due to the lower SEI formation detected at the higher carbonization temperature, as also shown by *ex situ* NMR.

Less pronounced quasi-metallic Na signal in the first cycle compared to the second, which can be seen in Fig. 11, is attributed to the loss of Na ions due to SEI formation in the first cycle as also indicated by a slight broadening of the signal around the electrolyte during first sodiation. Further broadening of the signal around the electrolyte during the first desodiation and throughout the second cycle, is attributed to the poor reversibility of Na ion insertion during the desodiation in HC1600. The primary reason for the low reversibility at higher carbonization temperatures, is the trapping of Na ions between the graphene sheets, yielding the NMR signal around 300 ppm even after desodiation [7]. This observation is related to the reversible sp^2 hybridized C content changes in hard carbon structure during sodiation, as illustrated in Fig. 3 for HC900, and the non-reversible changes at HC1600.

To summarize, the performance of hard carbons as anodes in sodium-ion batteries (SIBs) is influenced by carbonization temperatures which primarily affects the structural properties and the formation of the SEI layer. High-temperature carbonization (e.g. HC1600) yields more ordered structures with an overall lower amount of SEI, ensuring good capacity retention and consistent cycling stability. Low amount of defects and a very rigid carbon lattice lead to lower capacity and poorer reversibility of sodium ion insertion, as the adsorption and insertion of Na ions are no longer prevalent. Low-temperature carbonization (e.g. HC900) produces flexible, disordered structures, allowing reversible sodium ion insertion but with less stable cycling performance.

4. Conclusion

By investigating hard carbon negative electrode materials carbonized at various temperatures, we aimed to characterize structural changes in C lattice and their correlation with Na ion insertion and

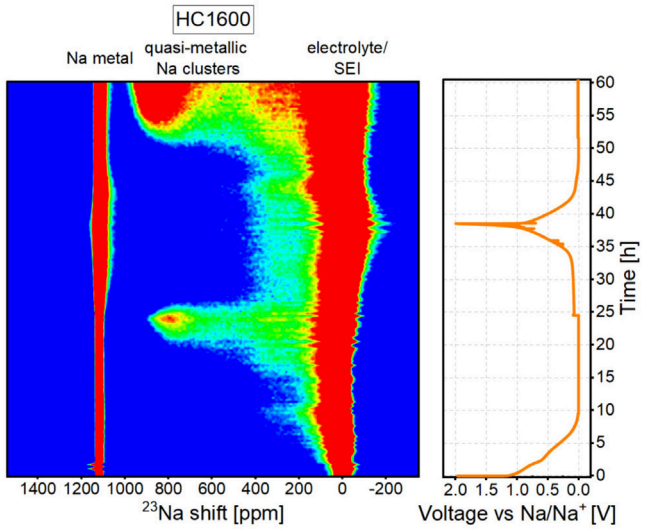

Fig. 11. Spectrum of solid-state ^{23}Na *operando* NMR on a Na-HC1600 half-cell at 90° orientation of electrodes with respect to the external magnetic field of the spectrometer. Electrochemistry is added on the right.

adsorption mechanisms during battery cycling. Analysis of C K-edge XRS spectra revealed that higher carbonization temperatures lead to an increase in sp^2/sp^3 hybridization ratio of material, indicating a transition towards a more graphitic structure with less defects, shorter C–C distances and enhanced long-range order. While this structural shift was confirmed by EXAFS analysis, it was not able to fully capture subtle changes in C–C distances.

Examining sp^2/sp^3 hybridized C atoms in pre-cycled battery samples showed a decrease in sp^2 hybridization during sodiation, particularly notable in HC900. This was attributed to the bending of graphitic layers to accommodate Na ions during insertion. At higher carbonization temperatures, a more consistent sp^2 ratio was maintained during sodiation/desodiation, primarily due to pore filling being the prevailing insertion mechanism. This was supported by *Operando* ^{23}Na NMR, which tracked the pore filling mechanism and confirmed its presence only at higher carbonization temperatures. Since *ex situ* methods are unable to observe Na in metastable states due to self discharge the observed change in sp^2 hybridization is only due to the Na insertion and adsorption at defect sites.

The measured XRS Na K-edge spectra are well described with a linear combination of the NaF and Na_2CO_3 reference spectra, which are the main constituents of the SEI. The presence of any metallic or quasi-metallic Na in *ex situ* negative electrodes has been excluded. A systematic variation of the SEI composition during the sodiation and desodiation have been observed in agreement with XPS and *ex situ* NMR measurements. Besides changes in the SEI composition, a part of the observed variations in the measured XRS spectra were attributed to the insertion of Na ions and adsorption of Na at defect sites.

CRediT authorship contribution statement

Ava Rajh: Writing – review & editing, Writing – original draft, Methodology, Formal analysis, Data curation, Conceptualization. **Matej Gabrijelčič:** Writing – original draft, Methodology, Formal analysis, Data curation, Conceptualization. **Blaž Tratnik:** Methodology, Conceptualization. **Klemen Bučar:** Software, Methodology, Data curation. **Iztok Arčon:** Supervision, Formal analysis. **Marko Petric:** Methodology, Formal analysis. **Robert Dominko:** Supervision, Project administration, Funding acquisition. **Alen Vizintin:** Writing – original draft, Supervision, Methodology, Investigation, Conceptualization. **Matjaž Kavčič:** Writing – original draft, Supervision, Methodology, Investigation, Conceptualization.

Declaration of competing interest

The authors declare that they have no known competing financial interests or personal relationships that could have appeared to influence the work reported in this paper.

Acknowledgements

This research is part of the PhD "Unravelling the electrochemical mechanisms of battery degradation by operando NMR and X-ray absorption spectroscopy" supported by CERIC-ERIC. This research also received financial support from the Slovenian Research and Innovation Agency (ARIS) under research programs P1-0112, P2-0423 and projects N2-0266, J2-4462. Additionally, this research was supported by the NATO Science for Peace and Security (SPS) Programme under grant G5836-SUPERCAR.

We acknowledge DESY (Hamburg, Germany), a member of the Helmholtz Association HGF, for the provision of experimental facilities. Parts of this research were carried out at PETRA III and we would like to thank Hlynur Gretarsson and Martin Sundermann for assistance in using the P01 Beamline and for recording additional Na K-edge XRS spectrum for the NaF reference sample. Beamtime was allocated for proposal I-20221051 EC. We also thank Blanka Dethlefs from ID20@ESRF for performing the Na K-edge XRS measurement of metallic Na. We would like to thank the Slovenian NMR Centre for the use of their spectrometer as well as Andraž Krajnc and Uroš Javornik for their advice on the NMR measurements.

Appendix

A.1. Theoretical calculations

Sodium K-edge XAS spectra were calculated using first-principle quantum mechanical Density Functional Theory (DFT) calculations, with a Cp2k software package [58]. Calculations were primarily performed in a ground state approximation, though some were repeated in the linear response time-dependent regime (lr-TDDFT) to validate the use of the lower-level approximation. Our main model for Na insertion consisted of 128 carbon atoms arranged in two parallel planes, with applied periodic boundary conditions to simulate the rest of graphite crystal structure. Initially, cell optimization was performed on a pure carbon system. Na atoms were added between the layers and defects were introduced, such as a vacancy in the carbon lattice or a substitution of a carbon atom with an oxygen atom [12,59]. The structure was left to relax and the resulting atomic positions were used as a starting point for XAS calculations. For the Na K-edge spectra of reference compounds (NaCl and NaF), a similar procedure was followed, the unit cell with 64 atoms (32 Na and 32 Cl or F) was constructed and left to relax, then the XAS spectra were calculated using the lr-TDDFT procedure with a hybrid functional approach [60].

For geometry optimization, a polarized triple ζ basis set was used [61] for all atoms, along with a Goedecker–Teter–Hutter (GTH) pseudo potential. General gradient approximation Perdew–Burke–Ernzerhof (PBE) [62] potential was adopted for the exchange–correlation functional. In the XAS calculations, only the absorbing atom was described by an all electron polarization-consistent pc-3 basis set [63]. The transition probability was computed by including the core-hole potential on the absorbing atom. The core-hole effect was accounted for by employing a half-core hole scheme [64]. The resulting spectra were constructed by broadening the transition probabilities with a Gaussian function to mimic the experimental broadening. The spectra were then rigidly shifted 16.2 eV to match the experimental excitation energies (see Fig. A.12). The shift is a result of the chosen exchange correlation potential.

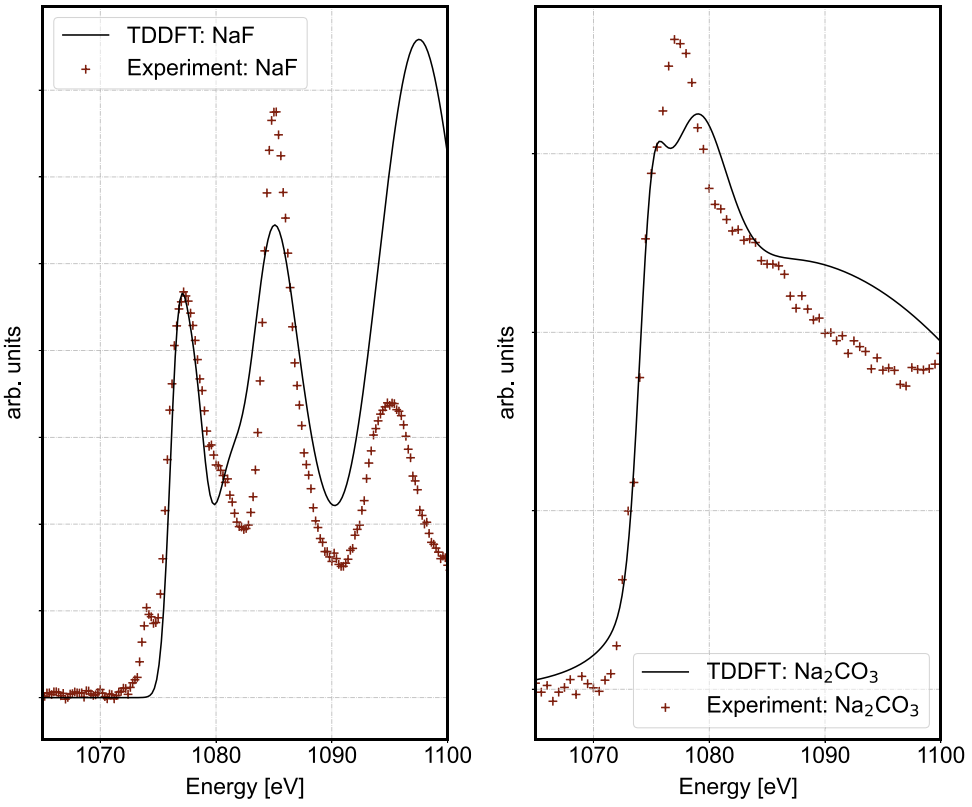

Fig. A.12. Comparison of (a) theoretical TDDFT calculations of NaF spectra with the experimental NaF and (b) TDDFT calculated Na_2CO_3 compared to the experimental one.

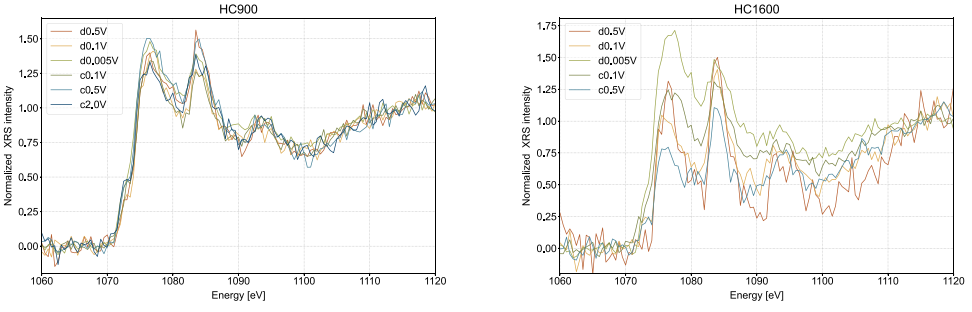

Fig. A.13. Variation in Sodium K-edge XRS spectra throughout the discharge and charge cycle of Na-ion battery. Pristine anode material was carbonized at 900 and 1600 °C respectively. The final anode in 1600 series was left out as the Na signal was very weak and it would obscure the rest of the spectra.

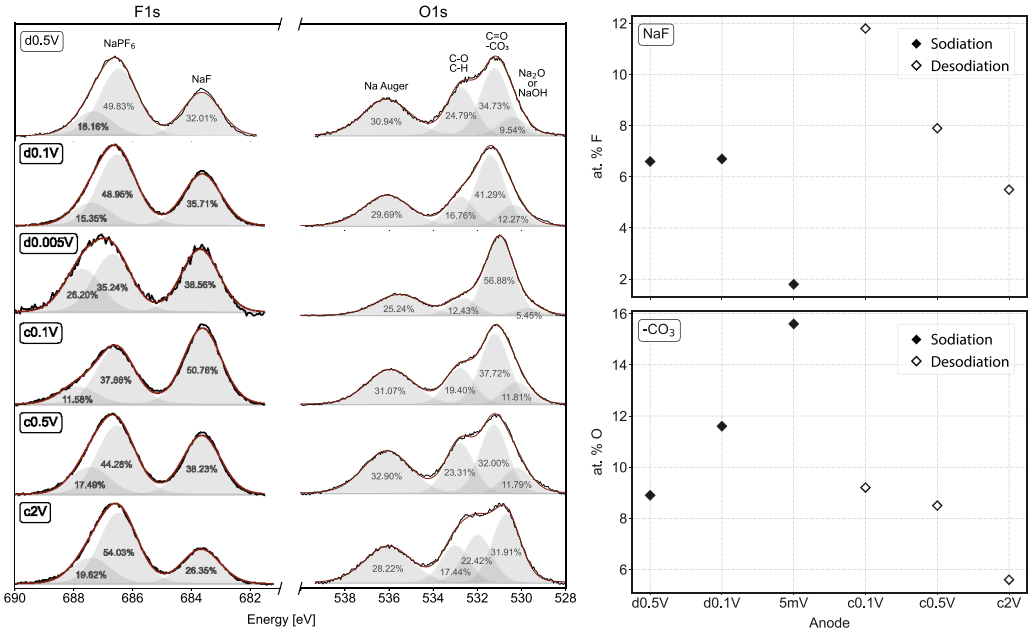

Fig. A.14. *Ex situ* XPS spectra of surface oxygen and fluorine species throughout the discharge and charge cycle of hard carbon carbonized at 900 °C. They show an increased presence of in SEI component Na_2CO_3 by the end of the discharge cycle, suggesting an increase in SEI formation with a simultaneous decrease in the trace of the electrolyte $NaPF_6$ left after washing the electrode. Full markers represent sodiation, empty represent desodiation.

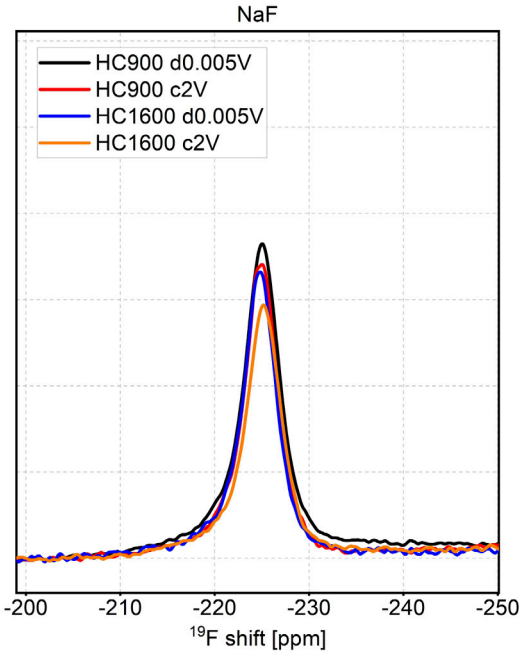

Fig. A.15. *Ex situ* solid-state ^{19}F ssNMR spectra of HC900 and HC1600 powder extracted in the discharged and charged state. It shows a consistent presence of F in all recorded points confirming the stability of the NaF component in the SEI during sodiation/desodiation.

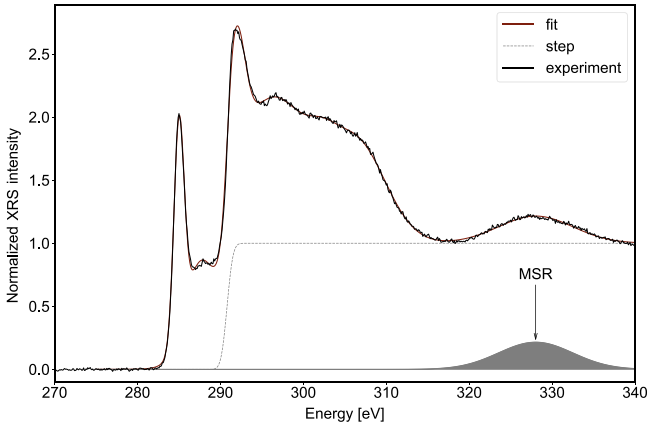

Fig. A.16. Carbon K-edge XRS spectrum of pristine hard carbon carbonized at 1600 °C. Red line represents a model, composed of 6 Gaussian functions (2 to describe the π region and 4 to describe the σ region). The Gaussian function used to fit the MSR region is represented by solid grey. (For interpretation of the references to colour in this figure legend, the reader is referred to the web version of this article.)

A.2. Sodium K-edge XRS

See Fig. A.13.

A.3. X-ray photoelectron spectroscopy (XPS)

Ex situ X-ray photoelectron spectroscopy (XPS) of the cycled HC900 electrode at different discharge and charge states was performed using the Versa probe 3 AD (Physical Electronics, Chanhassen, U.S.A) with a monochromatic Al Kα X-ray source operating at 15 kV and 13.3 mA. The cycled HC900 electrodes were put on a non-conductive double-sided scotch tape in the "floating" setup and placed in the centre of the XPS holder in a glove box filled with argon. The samples were transferred to the XPS intro chamber using a transfer vessel without exposure to air. Spectra were recorded for each sample by scanning a 1 × 1 mm area with a spot size of 200 μm. High-resolution spectra were measured at a pass energy of 27 eV and step of 0.05 eV, to obtain high quality data. Analysis of the peaks was performed with the Multipak software using a weighted sum of Lorentzian and Gaussian component curves after Shirley background subtraction. The binding energies were referenced to the internal gold standard.

A.4. Ex situ ^{19}F ssNMR

See Fig. A.15.

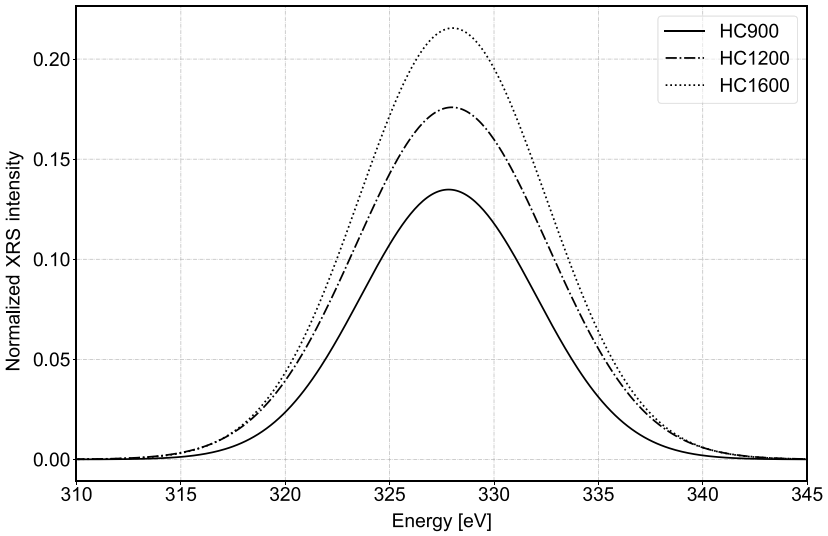

Fig. A.17. Gaussian functions describing the MSR peak of the carbon K-edge XRS spectra for three pristine hard carbon materials carbonized at 900, 1200 and 1600 °C.

A.5. MSR peak fit

See Figs. A.16 and A.17.

References

[1] Fei Xie, Zhen Xu, Zhenyu Guo, Maria-Magdalena Titirici, Hard carbons for sodium-ion batteries and beyond, Prog. Energy 2 (4) (2020) 042002.

[2] George Zhao Gaddam (Ed.), Handbook of Sodium-Ion Batteries: Materials and Characterization, Jenny Stanford Publishing, 2023.

[3] S. Komaba, T. Nakayama, A. Ogata, T. Shimizu, C. Takei, S. Takada, A. Hokura, I. Nakai, Electrochemically reversible sodium intercalation of layered NaNi 0.5Mn0.5O2 and NaCrO2, in: ECS Transactions - Intercalation Compounds for Energy Conversion and Storage Devices - 214th ECS Meeting, 2009, pp. 43–55.

[4] Long Wang, Yuhao Lu, Jue Liu, Maowen Xu, Jinguang Cheng, Dawei Zhang, John B. Goodenough, A superior low-cost cathode for a Na-ion battery, Angew. Chem. (Int. Ed. Engl.) 52 (7) (2013) 1964–1967.

[5] Haegyeom Kim, Jihyun Hong, Gabin Yoon, Hyunchul Kim, Kyu-Young Park, Min-Sik Park, Won-Sub Yoon, Kisuk Kang, Sodium intercalation chemistry in graphite, Energy Environ. Sci. 8 (10) (2015) 2963–2969.

[6] Kazuma Gotoh, 23Na solid-state NMR analyses for na-ion batteries and materials, Batter. Supercaps 4 (8) (2021) 1267–1278.

[7] Blaž Tratnik, Nigel Van de Velde, Ivan Jerman, Gregor Kapun, Elena Tchernychova, Matija Tomšič, Andrej Jamnik, Boštjan Genorio, Alen Vizintin, Robert Dominko, Correlating structural properties with electrochemical behavior of non-graphitizable carbons in Na-Ion batteries, ACS Appl. Energy Mater. 5 (9) (2022) 10667–10679.

[8] Th. Henning, Th, F. Salama, Carbon in the Universe, Science 282 (5397) (1998) 2204–2210.

[9] Sumio Iijima, Helical microtubules of graphitic carbon, Nature 354 (6348) (1991) 56–58.

[10] Uttam Mittal, Lisa Djuandhi, Neeraj Sharma, Henrik L. Andersen, Structure and function of hard carbon negative electrodes for sodium-ion batteries, J. Phys.: Energy 4 (4) (2022) 042001.

[11] Luis Kitsu Iglesias, Emma N. Antonio, Tristan D. Martinez, Liang Zhang, Zengqing Zhuo, Steven J. Weigand, Jinghua Guo, Michael F. Toney, Revealing the sodium storage mechanisms in hard carbon pores, Adv. Energy Mater. 13 (44) (2023) 2302171.

[12] Emilia Olsson, Jonathon Cottom, Qiong Cai, Defects in hard carbon: Where are they located and how does the location affect alkaline metal storage? Small 17 (18) (2021) 2007652.

[13] Zhaohua Wang, Xin Feng, Ying Bai, Haoyi Yang, Ruiqi Dong, Xinran Wang, Huajie Xu, Qiyu Wang, Hong Li, Hongcai Gao, Chuan Wu, Probing the energy storage mechanism of quasi-metallic Na in hard carbon for sodium-ion batteries, Adv. Energy Mater. 11 (11) (2021) 2003854.

[14] Ryohei Morita, Kazuma Gotoh, Mika Fukunishi, Kei Kubota, Shinichi Komaba, Naoto Nishimura, Takashi Yumura, Kenzo Deguchi, Shinobu Ohki, Tadashi Shimizu, Hiroyuki Ishida, Combination of solid state NMR and DFT calculation to elucidate the state of sodium in hard carbon electrodes, J. Mater. Chem. A 4 (34) (2016) 13183–13193.

[15] Ronnie Mogensen, Daniel Brandell, Reza Younesi, Solubility of the solid electrolyte interphase (SEI) in sodium ion batteries, ACS Energy Lett. 1 (6) (2016) 1173–1178.

[16] Fernando A. Soto, Pengfei Yan, Mark H. Engelhard, Asma Marzouk, Chongmin Wang, Guiliang Xu, Zonghai Chen, Khalil Amine, Jun Liu, Vincent L. Sprenkle, Fedwa El-Mellouhi, Perla B. Balbuena, Xiaolin Li, Tuning the solid electrolyte interphase for selective Li- and Na-ion storage in hard carbon, Adv. Mater. 29 (18) (2017) 1606860.

[17] Shinichi Komaba, Toru Ishikawa, Naoaki Yabuuchi, Wataru Murata, Atsushi Ito, Yasuhiko Ohsawa, Fluorinated ethylene carbonate as electrolyte additive for rechargeable Na batteries, ACS Appl. Mater. Interfaces 3 (11) (2011) 4165–4168.

[18] Bertrand Philippe, Mario Valvo, Fredrik Lindgren, Hakan Rensmo, Kristina Edström, Investigation of the electrode/electrolyte interface of Fe2O3 composite electrodes: Li vs Na batteries, Chem. Mater. 26 (2014).

[19] Gebrekidan Gebresilassie Eshetu, Sylvie Grugeon, Huikyong Kim, Sangsik Jeong, Liming Wu, Gregory Gachot, Stephane Laruelle, Michel Armand, Stefano Passerini, Comprehensive insights into the reactivity of electrolytes based on sodium Ions, ChemSusChem 9 (5) (2016) 462–471.

[20] Yongxin Huang, Luzi Zhao, Li Li, Man Xie, Feng Wu, Renjie Chen, Electrolytes and electrolyte/electrode interfaces in sodium-Ion batteries: from scientific research to practical application, Adv. Mater. (Deerfield Beach, Fla.) 31 (21) (2019) e1808393.

[21] Miguel A. Muñoz-Márquez, Maider Zarrabeitia, Elizabeth Castillo-Martínez, Aitor Eguía-Barrio, Teófilo Rojo, Montse Casas-Cabanas, Composition and evolution of the solid-electrolyte interphase in Na2Ti3O7 electrodes for Na-ion batteries: XPS and Auger parameter analysis, ACS Appl. Mater. Interfaces 7 (14) (2015) 7801–7808.

[22] Clement Bommier, Xiulei Ji, Electrolytes, SEI formation, and binders: A review of nonelectrode factors for sodium-ion battery anodes, Small 14 (16) (2018) 1703576.

[23] O. Wessely, Mikhail Katsnelson, O. Eriksson, Ab initio theory of dynamical core-hole screening in graphite from X-Ray absorption spectra, Phys. Rev. Lett. 94 (2005) 167401.

[24] Zulipiya Shadike, Enyue Zhao, Yong-Ning Zhou, Xiqian Yu, Yong Yang, Enyuan Hu, Seongmin Bak, Lin Gu, Xiao-Qing Yang, Advanced characterization techniques for sodium-ion battery studies, Adv. Energy Mater. 8 (17) (2018) 1702588.

[25] Christopher A. O'Keefe, Clare P. Grey, NMR investigations of sodium-ion batteries, in: Sodium-Ion Batteries, John Wiley & Sons, Ltd, 2022, pp. 215–257.

[26] Yue Pan, Yuzi Zhang, Bharathy S. Parimalam, Cao Cuong Nguyen, Guiling Wang, Brett L. Lucht, Investigation of the solid electrolyte interphase on hard carbon electrode for sodium ion batteries, J. Electroanal. Chem. 799 (2017) 181–186.

[27] Shinichi Komaba, Wataru Murata, Toru Ishikawa, Naoaki Yabuuchi, Tomoaki Ozeki, Tetsuri Nakayama, Atsushi Ogata, Kazuma Gotoh, Kazuya Fujiwara, Electrochemical Na insertion and solid electrolyte interphase for hard-carbon electrodes and application to Na-Ion batteries, Adv. Funct. Mater. 21 (20) (2011) 3859–3867.

[28] J. Diaz, O.R. Monteiro, Z. Hussain, Structure of amorphous carbon from near-edge and extended x-ray absorption spectroscopy, Phys. Rev. B 76 (9) (2007) 094201.

[29] Zhenbao Feng, Yangming Lin, Cunwei Tian, Haiquan Hu, Dangsheng Su, Combined study of the ground and excited states in the transformation of nanodiamonds into carbon onions by electron energy-loss spectroscopy, Sci. Rep. 9 (1) (2019) 3784.

[30] Winfried Schuelke, Winfried Schuelke, Electron Dynamics by Inelastic X-Ray Scattering, Oxford Series on Synchrotron Radiation, Oxford University Press, 2007.

[31] Laura de Kort, Masoud Lazemi, Alessandro Longo, Valerio Gulino, Henrik P. Rodenburg, Didier Blanchard, Christoph Sahle, Martin Sundermann, Hlynur Gretarsson, Ad M. J. van der Eerden, Hebatalla Elnaggar, Frank M.F. de Groot, Peter Ngene, Deciphering the origin of interface-induced high Li and Na Ion conductivity in nanocomposite solid electrolytes using X-Ray Raman spectroscopy, Adv. Energy Mater. 2303381.
[32] Ava Rajh, Iztok Arčon, Klemen Bučar, Matjaž Žitnik, Marko Petric, Alen Vizintin, Jan Bitenc, Urban Košir, Robert Dominko, Hlynur Gretarsson, Martin Sundermann, Matjaž Kavčič, Characterization of electrochemical processes in metal-organic batteries by X-ray Raman spectroscopy, J. Phys. Chem. C 126 (12) (2022) 5435–5442.
[33] J. Sahle, A. Mirone, J. Niskanen, J. Inkinen, M. Krisch, S. Huotari, Planning, performing and analyzing X-ray Raman scattering experiments, J. Synchrotron Radiat. 22 (2) (2015) 400–409.
[34] Ch J. Sahle, A. Mirone, T. Vincent, A. Kallonen, S. Huotari, Improving the spatial and statistical accuracy in X-ray Raman scattering based direct tomography, J. Synchrotron Radiat. 24 (2) (2017) 476–481.
[35] Pierre Gueriau, Jean Pascal Rueff, Sylvain Bernard, Josiane A. Kaddissy, Sarah Goler, Christoph J. Sahle, Dimosthenis Sokaras, Roy A. Wogelius, Phillip L. Manning, Uwe Bergmann, Loïc Bertrand, Noninvasive Synchrotron-Based X-ray Raman Scattering Discriminates Carbonaceous Compounds in Ancient and Historical Materials, Anal. Chem. 89 (20) (2017) 10819–10826.
[36] K. Hämäläinen, S. Manninen, Resonant and non-resonant inelastic x-ray scattering, J. Phys.: Condens. Matter. 13 (34) (2001) 7539.
[37] Michael Krisch, Francesco Sette, X-Ray Raman scattering from low z materials, Surf. Rev. Lett. 09 (02) (2002) 969–976.
[38] Sunil K. Sinha, Theory of inelastic X-Ray scattering from condensed matter, J. Phys.: Condens. Matter. 13 (34) (2001) 7511.
[39] Clement Bommier, Todd Wesley Surta, Michelle Dolgos, Xiulei Ji, New mechanistic insights on Na-Ion Storage in nongraphitizable carbon, Nano Lett. 15 (9) (2015) 5888–5892.
[40] Oliver Pecher, Javier Carretero-González, Kent J. Griffith, Clare P. Grey, Materials' methods: NMR in battery research, Chem. Mater. 29 (1) (2017) 213–242.
[41] S. Huotari, Ch J. Sahle, Ch Henriquet, A. Al-Zein, K. Martel, L. Simonelli, R. Verbeni, H. Gonzalez, M.C. Lagier, C. Ponchut, M. Moretti Sala, M. Krisch, G. Monaco, A large-solid-angle X-ray Raman scattering spectrometer at ID20 of the European Synchrotron Radiation Facility, J. Synchrotron Radiat. 24 (2017) 521–530.
[42] Matthew Newville, Larch: An analysis package for XAFS and related spectroscopies, J. Phys. Conf. Ser. 430 (2013) 012007.
[43] S.G.J. van Meerten, W.M.J. Franssen, A.P.M. Kentgens, ssNake: A cross-platform open-source NMR data processing and fitting application, J. Magn. Reson. 301 (2019) 56–66.
[44] Anja Aarva, Volker L. Deringer, Sami Sainio, Tomi Laurila, Miguel A. Caro, Understanding X-ray spectroscopy of carbonaceous materials by combining experiments, density functional theory, and machine learning. part II: Quantitative fitting of spectra, Chem. Mater. 31 (22) (2019) 9256–9267.
[45] Anja Aarva, Volker L. Deringer, Sami Sainio, Tomi Laurila, Miguel A. Caro, Understanding X-ray spectroscopy of carbonaceous materials by combining experiments, density functional theory, and machine learning. Part I: Fingerprint spectra, Chem. Mater. 31 (22) (2019) 9243–9255.
[46] Rafaella Georgiou, Christoph J. Sahle, Dimosthenis Sokaras, Sylvain Bernard, Uwe Bergmann, Jean-Pascal Rueff, Loïc Bertrand, X-Ray Raman scattering: A hard X-ray probe of complex organic systems, Chem. Rev. 122 (15) (2022) 12977–13005.
[47] Sami Sainio, Niklas Wester, Anja Aarva, Charles J. Titus, Dennis Nordlund, Esko I. Kauppinen, Elli Leppänen, Tommi Palomäki, Jessica E. Koehne, Olli Pitkänen, Krisztian Kordas, Maria Kim, Harri Lipsanen, Miran Mozetič, Miguel A. Caro, M. Meyyappan, Jari Koskinen, Tomi Laurila, Trends in carbon, oxygen, and nitrogen core in the X-ray absorption spectroscopy of carbon nanomaterials: A guide for the perplexed, J. Phys. Chem. C 125 (1) (2021) 973–988.
[48] H. Daniels, R. Brydson, B. Rand, A. Brown, Investigating carbonization and graphitization using electron energy loss spectroscopy (EELS) in the transmission electron microscope (TEM), Phil. Mag. 87 (27) (2007) 4073–4092.
[49] S.D. Berger, D.R. McKenzie, P.J. Martin, EELS analysis of vacuum arc-deposited diamond-like films, Phil. Mag. Lett. 57 (6) (1988) 285–290.
[50] Joshua M. Stratford, Phoebe K. Allan, Oliver Pecher, Philip A. Chater, Clare P. Grey, Mechanistic insights into sodium storage in hard carbon anodes using local structure probes, Chem. Commun. 52 (84) (2016) 12430–12433.
[51] D.G. McCulloch, R. Brydson, Carbon K-shell near-edge structure calculations for graphite using the multiple-scattering approach, J. Phys.: Condens. Matter. 8 (21) (1996) 3835–3841.
[52] Andrew J. Scott, Rik Brydson, Maureen MacKenzie, Alan J. Craven, Theoretical investigation of the ELNES of transition metal carbides for the extraction of structural and bonding information, Phys. Rev. B 63 (24) (2001) 245105.
[53] Alan J. Craven, Laurence A.J. Garvie, Electron energy loss near edge structure (ELNES) on the carbon K-edge in transition metal carbides with the rock salt structure, Microsc. Microanal. Microstruct. 6 (1) (1995) 89–98.
[54] M. Newville, P. Līviņš, Y. Yacoby, J.J. Rehr, E.A. Stern, Near-edge x-ray-absorption fine structure of Pb: A comparison of theory and experiment, Phys. Rev. B 47 (21) (1993) 14126–14131.
[55] John J. Rehr, Joshua J. Kas, Fernando D. Vila, Micah P. Prange, Kevin Jorissen, Parameter-free calculations of X-ray spectra with FEFF9, Phys. Chem. Chem. Phys. 12 (21) (2010) 5503–5513.
[56] Walter A. (Walter Ashley) Harrison, Electronic Structure and the Properties of Solids : The Physics of the Chemical Bond, Freeman, San Francisco, 1980.
[57] Camélia Matei Ghimbeu, Adrian Beda, Bénédicte Réty, Hamza El Marouazi, Alen Vizintin, Blaž Tratnik, Loic Simonin, Julie Michel, John Abou-Rjeily, Robert Dominko, Review: Insights on hard carbon materials for sodium-ion batteries (SIBs): Synthesis – properties – performance relationships, Adv. Energy Mater. 2303833.
[58] Thomas D. Kühne, Marcella Iannuzzi, Mauro Del Ben, Vladimir V. Rybkin, Patrick Seewald, Frederick Stein, Teodoro Laino, Rustam Z. Khaliullin, Ole Schütt, Florian Schiffmann, Dorothea Golze, Jan Wilhelm, Sergey Chulkov, Mohammad Hossein Bani-Hashemian, Valéry Weber, Urban Borštnik, Mathieu Taillefumier, Alice Shoshana Jakobovits, Alfio Lazzaro, Hans Pabst, Tiziano Müller, Robert Schade, Manuel Guidon, Samuel Andermatt, Nico Holmberg, Gregory K. Schenter, Anna Hehn, Augustin Bussy, Fabian Belleflamme, Gloria Tabacchi, Andreas Glöß, Michael Lass, Iain Bethune, Christopher J. Mundy, Christian Plessl, Matt Watkins, Joost VandeVondele, Matthias Krack, Jürg Hutter, CP2K: An electronic structure and molecular dynamics software package - Quickstep: Efficient and accurate electronic structure calculations, J. Chem. Phys. 152 (19) (2020).
[59] Kiyou Shibata, Kakeru Kikumasa, Shin Kiyohara, Teruyasu Mizoguchi, Simulated carbon K edge spectral database of organic molecules, Sci. Data 9 (1) (2022) 214.
[60] Augustin Bussy, Jürg Hutter, Efficient and low-scaling linear-response time-dependent density functional theory implementation for core-level spectroscopy of large and periodic systems, Phys. Chem. Chem. Phys. 23 (8) (2021) 4736–4746.
[61] Joost VandeVondele, Jürg Hutter, Gaussian basis sets for accurate calculations on molecular systems in gas and condensed phases, J. Chem. Phys. 127 (11) (2007) 114105.
[62] Xin Xu, William A. Goddard, The extended Perdew-Burke-Ernzerhof functional with improved accuracy for thermodynamic and electronic properties of molecular systems, J. Chem. Phys. 121 (9) (2004) 4068–4082.
[63] Frank Jensen, Polarization consistent basis sets: Principles, J. Chem. Phys. 115 (2001) 9113–9125.
[64] J.C. Slater, K.H. Johnson, Self-consistent-field α cluster method for polyatomic molecules and solids, Phys. Rev. B 5 (3) (1972) 844–853.